Progressive development of E-W extension across the Tibetan plateau: A case study of the Thakkhola graben, west-central Nepal

Alex D. Brubacher[1], Kyle P. Larson[1]*, John M. Cottle[2], William Matthews[3], Alfredo Camacho[4]

[1]Department of Earth, Environmental and Geographic Sciences, University of British Columbia Okanagan, Kelowna, BC, Canada

[2]Department of Earth Science, University of California, Santa Barbara, CA, USA

[3]Department of Geoscience, University of Calgary, Calgary, AB, Canada

[4]Department of Geological Sciences, University of Manitoba, Winnipeg, MB, Canada

*Corresponding author: kyle.larson@ubc.ca

Abstract

The Thakkhola graben is a large-scale N-S striking, E-W structure located in west-central Nepal that was actively extending ca. 17 Myr ago. New multi-system geochronological data from the immediate footwall of the Dangardzong fault, the main graben-forming structure in the Thakkhola, outline decelerating cooling paths. The average cooling rate in the immediate footwall of the Dangardzong fault progressively decreases from 55 ± 10 ˚C/Ma in the early Miocene (~ 22-13 Ma, monazite U-Th/Pb, mica $^{40}Ar/^{39}Ar$ and zircon U-Th/He), to 23 ± 8 ˚C/Ma in the middle to late Miocene (~13-8 Ma, zircon and apatite U-Th/He), and finally to 10 ± 2 ˚C/Ma from 8 Ma to present day (cooling post apatite U-Th/He closure). The deceleration in cooling rate is interpreted to reflect the widespread development of N-S striking graben structures in the Tibetan plateau in the middle Miocene and the progressive partitioning of strain away from the Thakkhola into other, younger, extensional features.

1. Introduction

In large continent-continent collisional zones such as the Himalaya-Tibet system, the locus of strain accommodation migrates to facilitate continued tectonic convergence under changing boundary conditions. A dynamic complexity often documented in these systems is the presence of significant extensional deformation, often occurring later in the orogenic history (e.g. Andersen & Jamtveit, 1990; Constenius, 1996; Dewey, 1988; Platt & Vissers, 1989; Teng, 1996). At present, the Himalayan-Tibetan system includes both actively shortening and extending kinematics (Yin, 2006; Yin & Harrison, 2000) and as such it provides an opportunity to study the transition/interactions between these processes during orogenesis. Late-stage, orogen-parallel E-W extension across the region has resulted in the development of numerous strike-slip faults and N-S striking graben in Tibet (Armijo et al., 1986; Fu et al., 2018; Jessup et al., 2008; Ratschbacher et al., 2011; Yin et al., 1999), some of which cut across the High Himalaya (Fig. 1A). The timing and mechanism(s) that drive orogen-parallel (E-W) extension in an actively N-S converging orogen, however, are poorly understood (e.g. Cottle et al., 2009). Initiation of these structures is broadly coincident with a shift in the locus of active thrusting from the Main Central thrust to the Main Boundary thrust (Leloup et al., 2010), fluctuations in monsoon intensity (Clift et al., 2008; Sun & Wang, 2005), and gravitationally driven eastward escape of the lower crust in southeastern Tibet (Clark & Royden, 2000). This study seeks to elucidate the evolution and regional kinematic implications of these structures through the interpretation of new, detailed geochronological data that informs the rate of development of the Thakkhola graben of central Nepal (Figs. 1A, B), one of the largest N-S trending graben in the region.

1.1. This Study

Previous chronologic data from the footwall of the Thakkhola graben has been used to argue that at least part of the cooling history recorded therein reflects movement along the northwest-striking, east-dipping Dangardzong fault, which bounds its west side (Fig. 1A; Hurtado, 2002). This interpretation is based on cooling paths/curves derived from the integration of monazite and xenotime U-Pb isotope dilution thermal ionization mass spectrometry (ID-TIMS) ages, and multi-grain aliquot muscovite, biotite, and K-feldspar $^{40}Ar/^{39}Ar$ ages, and indicate significant denudation initiated suddenly ca. 17 Ma and was sustained until ca. 13 Ma. The current study expands upon Hurtado's (2002) work through characterization of the plutons exposed in the footwall of the fault using petrology, laser ablation-based U-Th/Pb monazite, single-grain muscovite and biotite $^{40}Ar/^{39}Ar$ geochronology and apatite and zircon U-Th/He geochronology to: 1) distinguish between potential contributions of pre-Thakkhola graben cooling/exhumation from that associated with the opening of the structure, and 2) compare the cooling history of the Thakhola graben with other E-W extensional structures across Tibet to identify regionally significant patterns and use these observations to inform the initiation and development of E-W kinematics across the region.

2. Geological Setting

Much of the topographic relief within the Tibetan plateau is the result of large-scale, late Miocene to Pliocene E-W extension of the crust that resulted in the formation of graben and associated strike-slip faults (Fig. 1A; Ratschbacher et al., 2011; Yin et al., 1999). A subset of the graben that developed as a result of E-W extension, including the Thakkhola graben, reach southward across the crest of the Himalaya to form deeply incised valleys and kilometer-scale sedimentary basins (Figs. 1A, B). The Thakkhola graben in part defines the upper Kali Gandaki valley of west-central Nepal, where the valley floor sits at an elevation of ~2500 m between the peaks of Dhaulagiri (8167 m) to the west and Annapurna (8091 m) to the east. The graben extends southward almost to the South Tibetan detachment system (STDS; Fig. 1A), while its northern extent approaches the Indus-Tsangpo suture zone (Hodges, 2000; Hurtado et al., 2001). The main graben-forming structure, the NNW striking, steeply ENE-dipping Dangardzong normal fault defines the western side of the graben while the eastern boundary is defined by a series of unnamed, steeply west-dipping normal faults (Fig. 1B Colchen, 1999; Hurtado et al., 2001).

The footwall of the Dangardzong fault comprises generally low-metamorphic grade to unmetamorphosed rocks of the Tibetan sedimentary sequence (TSS) and two large granitic bodies (Colchen, 1999; Fort et al., 1982). The 'Mustang granite' of Hurtado (2002), herein referred to as the Mustang orthogneiss (see section 3.2.1), occurs to the north where it forms a half circle in map-pattern, cut by the Dangardzong fault to the east. The (Dolpo-) Mugu batholith to the south is a large, elongate, NW-SE trending body (Fig. 1B; Hurtado, 2002; Le Fort & France-Lanord, 1994). The Mustang and Mugu bodies have similar mineral assemblages to other leucogranite plutons that occur near the crest of the Himalaya, which are interpreted to be derived from partial melting of a metasedimentary source (Deniel et al., 1987; Le Fort et al., 1987; Searle et al., 2010). Existing age estimates for the bodies come from the Dhanggna Khola area of the Upper Mustang region (Fig. 1B) where monazite ID-TIMS analyses from the deformed Mustang orthogneiss yields a maximum age of 23.4 ± 0.2 Ma while undeformed dikes of interpreted Mugu affinity, which cross-cut the Mustang orthogneiss, provide a minimum age of 20.8 ± 0.7 Ma (Hurtado, 2002). Additionally, Harrison et al. (1997) reported an ion microprobe age of 17.6 ± 0.3 Ma for a specimen of presumed Mugu affinity farther south, near Ghar Gompa (Fig. 1B), however, no description of the specimen or outcrop was published.

The hanging wall of the Dangardzong fault includes a series of ~N-S trending syn-sedimentary normal faults that variably crosscut at least five graben-fill sedimentary formations, confirming protracted E-W extension (Colchen, 1999; Fort et al., 1982; Hurtado et al., 2001; Garzione et al., 2003). The oldest sedimentary unit that crops out within the graben has been dated using magnetostratigraphy to between ~11.0 and ~9.6 Ma (Garzione et al., 2000) and provides a minimum age for initiation of extension or basin development. Approximately 40 km east of the graben, hydrothermal muscovite from a N-S trending brittle fracture, interpreted to represent early deformation related to E-W extension in the Thakkhola graben, gave an ^{40}Ar/^{39}Ar age of ~14 Ma, extending the minimum age constraint for the inception of E-W extension in the region to the mid-Miocene (Coleman & Hodges, 1995). Mid-Miocene extension is compatible with cooling data from the footwall of the main bounding fault (Hurtado, 2002) and ca. 17 Ma ^{40}Ar/^{39}Ar dates synkinematic with east-directed shear, interpreted to reflect initial opening of the graben (Larson et al., 2019).

2.1. Sampling Sites/Locations

Field sampling locations of granitic specimens associated with the Mugu batholith are shown in Figure 2. Field relationships at each site are highlighted in Figure 3 and are detailed below. Lithologies and associated mineral assemblages are summarized in Table 1 and Figure 4.

The outcrop investigated at Ghami (Fig. 2) exposes ~1 m wide undeformed leucogranite dikes and sills that crosscut the host TSS (Fig. 3A). Specimen GH17B is a specimen of Bt-bearing leucogranite dike collected at this location (Figs. 3A, 4). Sampling at Ghar Gompa was more extensive, with 6 specimens collected (Fig. 2; Table 1). Specimens GG10 (fine-grained garnet-tourmaline leucogranite), GG11 and GG12 (fine- to medium-grained tourmaline ± garnet leucogranite) were collected from outcrops at or near the contact between the main body of the Mugu batholith and the TSS (Figs. 3B, 4). Specimens GG01A (medium-grained two-mica leucogranite), GG01B and GG13 (both tourmaline ± garnet leucogranites) are also from the main body of the Mugu batholith, however, their contact relationship with the TSS was not observed.

Outcrops of the Mustang orthogneiss dominate the Dhanggna khola area; TSS rocks are not observed (Hurtado, 2002; Fig. 2). The Mustang orthogneiss is typically well-foliated, records pervasive ductile deformation and is cross cut by undeformed dikes associated with the Mugu batholith (Hurtado, 2002). The deformed Mustang orthogneiss crops out as a weathered, fine- to medium-grained, deformed two-mica orthogneiss (DK16; Fig. 3C; Table 1) that contains large K-feldspar augen and a strong foliation defined by aligned quartz and biotite (Fig. 4). At this location, the Mustang orthogneiss is cross-cut by a set of vertical ~1+ m wide coarse-grained, undeformed granitic dikes, which in turn are cut by horizontal, ~15 cm wide undeformed fine-grained tourmaline-bearing leucogranite dikes (DK15; Fig. 3C; Table 1). Specimen DK14 is a medium-grained to pegmatitic muscovite and tourmaline-bearing leucogranite (Table 1; Fig. 4) collected from an isolated outcrop and as such its relationship with the rest of the igneous phases present at Dhanggna khola is unknown.

3. Geochronology

3.1. Methods

Full details of the methods employed for each analysis type, along with data tables, are available in the accompanying Supporting Information. The geochronology of specimens GG10 and GG12 was originally reported in Lihter et al. (2020). The data from those specimens are discussed with the specimens below and associated data are replotted herein (Fig. 5) for consistency.

Monazite from seven specimens (GG01A, GG10, GG12, DK14, DK15, DK16, and GH17B) were dated using Laser Ablation Multicollector Inductively Coupled Plasma Mass Spectrometry (LA-MC-ICP-MS) at the University of California, Santa Barbara following methods described in Cottle et al., (2012). Specimens were first crushed and ground using standard mechanical methods, and heavy minerals were separated using a Rogers Gold™ table, heavy liquids (Methyl iodide, MI, 3.35 g/cm^3), and Frantz™ magnetic techniques. Monazite were mounted in epoxy, polished to expose crystal centers and then analysed.

$^{40}Ar/^{39}Ar$ analyses were completed at the University of Manitoba using a laser (for step-heating) attached to a multi-collector mass-spectrometer. Mica grains were hand-picked from each specimen and visually checked for lack of inclusions and alteration. Micas were analysed as single grains to avoid potential problems with age homogenization during step-heating due to intergrain variability and grain size.

U-Th/He analyses of apatite and zircon were carried out at the University of Calgary through whole grain dissolution methods. Specimens were crushed and separated using standard procedures. Individual grains were hand-picked for analysis with preference given to high purity euhedral inclusion-free crystals. Analysis of zircon grains was carried out at the Colorado University Institute for Arctic and Alpine Research.

3.2. Monazite U-Th/Pb Geochronology

U-Th/Pb monazite geochronology (Table S1) was used to assess the crystallization age of the Mugu and Mustang bodies. Monazite in these specimens typically record a range of dates (Fig. 5). We, therefore, follow the approach of Lederer et al. (2013) and Larson et al. (2017) wherein the latest crystallization age of each specimen is estimated using the weighted mean age of the youngest identifiable sub-population of monazite. The resulting ages, quoted at 2SE, are used as the points in time from which the cooling path of the granite bodies initiated. All ages reported are calculated from the $^{232}Th/^{208}Pb$ system to avoid potential problems with excess ^{206}Pb from the decay of unsupported ^{230}Th (e.g., Schärer, 1984).

Forty monazite crystals from specimen GH17B (Ghami; Fig. 2) yield a crystallization age of ca. 22.0 ± 0.2 Ma, (MSWD = 1.2; Fig. 5A). Three specimens of the Mugu batholith were dated from the Ghar Gompa location (GG01A, GG10, and GG12; Fig. 2, Fig. 5B-D). The data from GG10 and GG12 were first reported in Lihter et al. (2020) and are replotted here. Monazite from specimen GG01A define a minimum crystallization age of 21.6 ± 0.1 Ma, (MSWD = 1.7; Fig. 5B), while those from GG10 and GG12 yield ages of 20.3 ± 0.2 Ma (MSWD = 1.1; Fig. 5C) and 21.4 ± 0.2 Ma (MSWD = 1.4; Fig. 5D), respectively.

Three specimens (DK14, DK15 and DK16) were collected from the Dhanggna Khola location for monazite geochronology (Fig. 2, Fig. 5E-G). Monazite from the pegmatitic specimen DK14 yield a minimum crystallization age of 26.1 ± 0.3 Ma (MSWD = 1.0; Fig. 5E). Monazite from specimen DK15, sampled from a dike that crosscuts the Mustang orthogneiss, define a minimum crystallization age of 22.2 ± 0.4 Ma (MSWD = 1.2; Fig. 5F). Finally, monazite from specimen DK16, a sample of the Mustang orthogneiss, yield a minimum age of 24.9 ± 0.7 Ma (MSWD = 0.4; Fig. 5G).

3.2.1 Paleozoic Populations

The monazite data from both DK14 and DK16 contain significant Paleozoic populations that range between ca. 450 and 500 Ma (Figs. 5E, G). The Paleozoic population in the Mustang orthogneiss (DK16) is interpreted to reflect the age of a granitic protolith. Similar age orthogneiss has been described from south of the Upper Mustang region in the high metamorphic grade rocks of the Greater Himalayan sequence (483.6 ± 9.1; Godin et al., 2001) and in other regions across the orogen (e.g. Gehrels et al., 2006a, 2006b). The interpreted youngest age for the deformed Mustang orthogneiss specimen reported herein is ca. 24.9 ± 0.7 Ma, while that of DK14, which is undeformed, is older at 26.1 ± 0.3 Ma. This indicates that deformation of the body may predate ca. 26 Ma, which is significantly different than previous interpretations that suggested it was younger than 23.4 ± 0.2 Ma (Hurtado, 2002). Because DK14 is undeformed, the Paleozoic sub-population (Fig. 5E) is thought to be inherited. The pegmatitic muscovite and tourmaline-bearing leucogranite may be derived from partial melting of the Mustang orthogneiss during high-grade metamorphism/anatexis.

3.3. Mica ^{40}Ar/^{39}Ar Geochronology

The results of ^{40}Ar/^{39}Ar single crystal step-heating analyses are presented in Figure 6 and reported in Table 2 (step-heating data are presented in Table S2). All specimens analyzed returned nearly flat age spectra that define a narrow range of ages from 15.7 ± 0.1 Ma to 17.2 ± 0.1 Ma, averaging ca. 88% of ^{39}Ar released. Closure temperatures (Table 2) were estimated separately for each specimen using the approach of Dodson (1973). Diffusion and activation energy parameters used for muscovite and biotite closure temperature calculations are those of Harrison et al. (2009) and Grove and Harrison (1996), respectively, assuming the same geometries used therein. Uncertainties in all parameters, including grain size, were propagated through the calculation.

Biotite from the granitic Mugu-affinity dike at the Ghami location, GH17B, yields an age of 16.1 ± 0.1 Ma with 100% of ^{39}Ar released (Fig. 6A).

Muscovite grains from several outcrops of the main body of the Mugu batholith at the Ghar Gompa location were analyzed (Fig. 6B). ^{40}Ar/^{39}Ar results for specimens GG10 and GG12 are reported in Larson et al. (2019), and yielded ages of 16.7 ± 0.1 and 16.9 ± 0.1 Ma, respectively. Specimens GG01A and GG01B, two medium-grained granites, both from the northeastern part of the Ghar Gompa area (Fig. 2), yield indistinguishable ages of 17.1 ± 0.1 and 16.9 ± 0.1 Ma at 81% and 96.2% of ^{39}Ar released, respectively (Fig. 6B). Specimen GG11 was sampled at the highest elevation reached at Ghar Gompa (Fig. 2). It is also a medium-grained granite and yields an age of 16.8 ± 0.1 Ma at 97.5% of ^{39}Ar released, indistinguishable from the neighboring specimens (Fig. 6B). Finally, specimen GG13, a medium-grained granite, also centrally located in the Ghar Gompa area (Fig. 2), yields a muscovite age of 15.7 ± 0.1 Ma at 98.3% of ^{39}Ar released (Fig. 6B).

At the Dhanggna Khola location (Fig. 2) muscovite from the fine-grained Mugu granite dike, specimen DK15, yields a plateau age of 17.2 ± 0.1 Ma at 88.1% of ^{39}Ar released (Fig. 6C). Muscovite from the pegmatitic alkali-feldspar granite, specimen DK14, gives a slightly 'saddle'-shaped release spectra, with a middle plateau at 17.1 ± 0.1 Ma at 59.4% ^{39}Ar released (Fig. 6C).

Because the ^{40}Ar/^{39}Ar ages are consistently younger than the U-Th/Pb monazite crystallization ages for corresponding specimens, they are interpreted to reflect cooling of the rocks after emplacement. The 'saddle'-shape spectrum in specimen DK14 may indicate the presence of excess Ar at grain margins (Lanphere & Dalrymple, 1976). Nevertheless, the age of the plateau portion of the spectrum is within uncertainty of the plateau ages of the other specimens and is, therefore, considered to be geologically meaningful.

3.4. U-Th/He Thermochronometry of Zircon and Apatite

Calculated dates, U and Th content, effective U (eU), and effective radii for individual zircon and apatite grains are summarized in Table 3; full data are presented in Table S3. Data for individual grains are presented in log-ratio plots (Vermeesch, 2010) created using the IsoplotR software of Vermeesch (2018). Where available, the central age (Fig. 7), which is the age corresponding to the geometric mean U-Th/He composition from a single sampling location, is taken as the preferred age, as it is considered the most accurate way to obtain an average of multiple single-crystal U-Th/He analyses (Vermeesch, 2008). An exception to this is the zircon cooling data from the Ghar Gompa location, where only 2 crystals yield reliable analyses. There, the reported age is the geometric mean.

Effective closure temperatures for zircon and apatite at each site were calculated using the approach of Dodson (1973) with the diffusivities and geometries as in Cherniak et al. (2009). Average grain sizes for each site were calculated, with uncertainty, to determine the closure temperature. Closure temperatures calculated parallel and perpendicular to the *c*-axis for zircon were within uncertainty and are therefore also averaged. Closure temperatures are reported in Table 3.

Both zircon and apatite U-Th/He results yield over-dispersed dates (Fig. 7). Overdispersion in U-Th/He dates may result from a number of factors such as undetected U- or Th- bearing inclusions or fractures, variations in grain size and/or chemical zonation contributing to an inaccurate alpha-ejection (FT) correction (Fitzgerald et al., 2006), or variations in diffusion kinetics resulting from radiation damage (Shuster et al., 2006). The quality and size of zircon and apatite crystals available for this study varied significantly from specimen to specimen. Inclusions may have been present in some of the grains analyzed despite efforts to avoid selecting such crystals, which may contribute to the overdispersion apparent in Figure 7. In addition, FT correction factors fail to account for U and Th zoning in crystals (Meesters & Dunai, 2002). The whole-grain U-Th/He analysis used in this study does not allow for the detection of chemical zoning within crystals, which may also have further contributed to overdispersion in the specimens analyzed. Finally, radiation damage can affect He diffusion in zircon and apatite. Its potential contribution to overdispersion can be investigated using eU (where eU = U + 0.235Th in ppm) as a proxy (Guenthner et al., 2013; Shuster et al., 2006).

Ellipses are colored according the eU concentration in each crystal in the logratio plots (Fig. 7), which allows for a qualitative check for possible eU-age correlation due to alpha-ejection track concentrations (Shuster et al., 2006). All zircon and apatite U-Th/He analysis presented, however, lack an eU-age correlation and thus radiation damage is likely not a major source of overdispersion in the log-ratio plots.

Four zircon crystals separated from the Mugu granite dike (GH17B) at the Ghami site define a central age of 10.3 ± 1.8 Ma (Fig. 7A). Unfortunately, GH17B did not contain useable apatite crystals. Two zircon grains picked from Ghar Gompa Mugu granite specimens (grains GG01B_1 and GG11_3) yielded U-Th/He ages that yield a geometric mean of 11.3 ± 0.3 (Fig. 7B). Zircon GG01B_2 from the same site gave a U-Th/He age of 43.6 ± 3.6 Ma, older than the U-Th/Pb age of the specimen before alpha-ejection correction and is thus discarded. The 15 apatite analyses from the Ghar Gompa site (from specimens GG01A, GG10, and GG12) are combined into a single log-ratio plot that yields a central age of 7.8 ± 1.3 Ma (Fig. 7C).

Analysis of five zircon crystals from the coarse-grained to pegmatitic granite at Dhanggna Khola (specimen DK14) define a central age of 12.4 ± 3.8 Ma (Fig. 7D). Eleven combined apatite dates were obtained from specimens DK14 and DK15 from the same site, which yield a central age of 5.6 ± 0.8 (Fig. 7E). Apatite DK15_6 gave a U-Th/He age of 25.9 ± 0.6 Ma before alpha-ejection correction, which is discarded as it is older than the U-Th/Pb age from the same specimen.

4. Discussion

4.1. Cooling paths

This study presents the first zircon and apatite U-Th/He geochronological data from the Upper Mustang region of central Nepal. Unlike previous studies (e.g. Hurtado, 2002) these new data, along with the new $^{40}Ar/^{39}Ar$ and U-Th/Pb ages presented herein, facilitates, for the first time, the opportunity to extrapolate to lower temperatures the cooling history for the three sites investigated. Cooling paths were determined using the calculated closure temperatures for Ar-in-muscovite and biotite and He-in-zircon and apatite. The crystallization temperature of Mugu-related melt is assumed to be 700 ± 50 ˚C, typical of Himalayan leucogranites (e.g. Ayres & Harris, 1997; Copeland et al., 1990; Visonà & Lombardo, 2002), while 10 ± 10 ˚C is used for the present-day temperature, which encompasses approximate variation in average monthly temperatures in the Upper Mustang region ("Climate-Data.org," 2019). Where more than one age was reported for a site for a given mineral isotopic system, a weighted mean age was calculated using IsoplotR of Vermeesch (2018) as was as mean closure temperature.

The calculated cooling path for the Ghami site (Fig. 8) records a decreasing cooling rate through time, from 57 ± 10 ˚C/Ma between 22 Ma to 16 Ma and 32 ± 11 ˚C/Ma between 16 Ma and 10 Ma, to a slower rate of 16 ± 3 ˚C/Ma between 10 Ma and the present. The cooling path calculated for the Ghar Gompa site is 55 ± 13 °C/Ma from 20 Ma to 17 Ma, which is indistinguishable from a rate of 51 ± 6 ˚C/Ma between 17 Ma to 11 Ma (Fig. 8). The cooling rate decreases after the zircon U-Th/He constraint to 29 ± 12 ˚C/Ma from 11 to 8 Ma, and again to 9 ± 2 ˚C/Ma from 8 Ma to present. The initial cooling rate calculated for the Dhanggna Khola site is 42 ± 11 ˚C/Ma from 22 Ma to 17 Ma and 64 ± 52 ˚C/Ma from 17 Ma to 12 Ma (Fig. 8). The large uncertainty in the rate between Ar-in-muscovite and He-in-zircon closure reflects the uncertainty in the central age of the zircon. Between 12 and 6 Ma the rate is calculated to be 17 ± 10 ˚C/Ma which decreases to a rate of 11 ± 3 ˚C/Ma from 6 Ma to present.

The earliest (~22 to ~16 Ma) portion of the cooling path at all locations ranges from 57 - 42 ˚C/Ma. That is similar to the cooling rate of 45 ˚C/Ma during this same time interval calculated by Hurtado (2002). However, the younger portions of the new and previously published cooling paths diverge. The new zircon U-Th/He ages presented herein indicate slower cooling rates in the post-mica cooling interval than that interpreted from $^{40}Ar/^{39}Ar$ K-feldspar data by Hurtado (2002). Despite the absolute differences between low temperature cooling rates, both paths show a significant slowdown in the middle Miocene.

Simple conductive cooling models can provide insight on the expected and/or geologically realistic cooling histories of intrusive bodies. The models of Jaeger (1964, 1968) incorporate intrusion temperature, size and geometry with background temperature and diffusivity to model conductive cooling. The cooling paths outlined above cannot be reproduced through passive cooling, i.e. cooling in place after intrusion, of the Mugu body at Ghar Gompa. The geometry of the Mugu pluton, which has a width of ~ 25 km and a length in excess of >100 km, was approximated as an infinite dyke with a starting temperature of 700 ± 50˚C (see above) and a country rock temperature of ~450 ˚C (see Lihter et al., 2020). Given those starting conditions, and a diffusivity of 0.5 mm^2s^{-1} (Whittington et al., 2009), the temperature at the margin of the pluton is predicted to be 571 ˚C at the time of Ar closure (see Table 2). The modelled cooling history is significantly slower than the observed along the lower temperature (<17 Ma) portion of the path, even if the background temperature is decreased to 0 ˚C at the time of Ar closure and the diffusivity is increased to 1 mm^2s^{-1} (see '2-stage model' Fig. 8). The same problem exists if the pluton modelled to intrude into rocks with a background temperature of 0˚C and a ‘fast’ diffusivity (1 mm^2s^{-1}). After fast initial cooling that broadly matches the observed, the predicted path slows such that the cooling rate is much slower than the observed (Fig. 8). The same basic pattern emerges when modelling the cooling of the Mugu pluton using the SILLS program of Nabelek et al. (2012). The model predicts a temperature of ~469 ˚C at the edge of the pluton at the time of Ar closure, indistinguishable from those calculated (Table 2), after which cooling of the model is slower than the observed path.

While it is possible for models to reproduce the initial cooling of the pluton from crystallization to Ar closure, the lack of fit at lower temperatures likely reflect the effect of exhumation, which is entirely unaccounted for. Interestingly, the point at which the model deviates from the observed cooling pattern coincides with initiation of extension in the Thakkhola graben at ca. 17 Ma (Hurtado, 2002; Larson et al., 2019). We suggest, therefore, that the evolution of the graben had a first-order effect on the cooling of the Mugu pluton.

4.2. E-W extension in the Thakkhola graben and the Tibetan plateau

Movement on the STDS, an orogen-scale extensional fault system that detached the upper and middle portions of the crust in the Himalaya, ceased by ~22 Ma in the Annapurna/Mustang region (Godin et al., 2001). Therefore, the cooling rates determined in this study are inferred to be unrelated to any potential exhumation driven by movement on the STDS. The cooling rates calculated for all three study locations (Ghami, Ghar Gompa, Dhanggna Khola; Fig. 2) are relatively invariant from ~22 to ~13 Ma, while a distinct decrease occurs between ~13 and ~8 Ma (Fig. 8). This slower cooling rate likely reflects one of the following three scenarios: 1) a reduction in regional erosion rates; 2) an overall decrease in E-W extension across Tibet or; 3) the initiation of extensional structures elsewhere in the Himalaya and the

Tibetan plateau that accommodate E-W extension, partitioning deformation away from Thakkhola region at this time.

In the first scenario, if the climate of the Tibetan plateau and the Thakkhola graben became drier, perhaps related to raising of the High Himalaya and development of an orographic barrier, erosion rates would be expected to decrease as the plateau became more arid, which would in turn decrease the rate of exhumation of the Thakkhola graben. Paleoclimatic studies, however, demonstrate that the intensity of the Asian monsoon was high during ~12-15 Ma (Sun & Wang, 2005), as was Himalayan erosion (Clift et al., 2008). In fact, it appears that erosion was rapid across much of southern Tibet in the early Miocene time (e.g. Carrapa et al., 2014; Copeland et al., 1995; Dai et al., 2013; Shen et al., 2016). Thus, if erosion was driving exhumation in the Thakkhola graben, it would be expected that the cooling rate would have increased, which we do not observe (Fig. 8). Consequently, exhumation, driven primarily by E-W extension, is the most plausible explanation.

The second scenario for the slowing of cooling rates observed in the Thakkhola graben is related to a decrease in E-W extension across southern Tibet with time. Molnar and Stock (2009) documented a reduction in convergence rate between India and Asia between ~20 and ~10 Ma. If E-W extension is related to N-S convergence, as has been proposed (e.g. Clark & Royden, 2000), a decline in convergence rate would also result in a decrease in the magnitude of E-W extension, assuming coupling between the middle and upper crust at this time (e.g. Larson et al., 2019). The total number of graben and related structures throughout Tibet, however, appears to increase with time culminating at the present day (Fig. 9; Ratschbacher et al., 2011).

The observation that the number of graben appear to increase with time favors the third scenario; strain partitioning away from the Thakkhola graben and into other E-W extension graben and associated structures. The timing of the initiation of graben structures in Tibet is summarized in Figure 9 and Table 4.

The early Miocene initiation of E-W extension across the Thakkhola graben is coeval with similar records elsewhere across the Himalaya and Tibet. Cooper et al. (2015) documented E-W extension in the Yadong Cross structure (YCS) by ~14 Ma (Fig. 9A), Mitsuishi et al. (2012) interpreted ductile E-W extension to have initiated with granite emplacement ca. 19 Ma in the Kung Co area of southern Tibet, and Murphy and Copeland (2005) provided evidence of E-W extension contemporaneous with N-S shortening in the Gurla Mandhata region at ≤ 15 Ma (Fig. 9A). Finally, in NW India, Thiede et al. (2006) interpreted rapid exhumation of the Leo-Pagril dome, beginning at ca. 16 Ma, to reflect the initiation of E-W extension.

In addition to the studies that recognized early Miocene E-W extension discussed above (Fig. 9A), others document the regional initiation of ductile and brittle E-W extensional structures at ~13-8 Ma (Table 4) for at least 8 different locations (Fig. 9B). Further work documents a second period of extension facilitated by brittle structures in the same locations at ~6-4 Ma (Table. 4; Fig. 9C). For example, Cottle et al., (2009) recognize a period of ductile E-W extension in the Ama Drime region at ~12 Ma, and initiation of related brittle extension in the same area at ~6-4 Ma (Jessup et al., 2008) (Table 4). North of the Kung Co rift, in the Tangra Yum Co rift (Fig. 9B), Dewane et al. (2006) outline two periods of E-W extension based on cooling path inflections at ~13 Ma and ~6 Ma. Finally, Ratschbacher et al. (2011) provide a summary of rifting in southern Tibet and show that early ductile E-W extensional structures consistently initiate at ~13-8 Ma, with a second population of brittle E-W structures that initiate around ~4-5 Ma. These studies, and the cooling rates defined herein, add to a growing body of evidence indicating a shift in orogen-wide kinematics initiated around 13-8 Ma, with perhaps further reorganization at ~5 Ma.

Graben development may be diachronous, with those farthest south and closest to the Himalaya, initiating first at ≥14 Ma, and those farther north initiating later (Fig. 9). This progression is outlined in the Yadong-Gulu system, as well as the Ama Drime - Xainze Dinggye system, where early extension is documented in the southern portions of the rifts and advances progressively northward (Fig. 9). Unfortunately, the timing of many of these structures is only bracketed by a maximum or minimum age and more detailed studies, using multiple thermochronometers, are required to precisely outline the timing of formation of these individual structures, and detailed progressive spatial development.

5. Conclusions

This study provides new geochronological information that detail the development of the Thakkhola graben in central Nepal. New U-Th/He data, together with $^{40}Ar/^{39}Ar$ dating of muscovite and biotite and U-Th/Pb dating of monazite, outline the cooling path for three locations in the footwall of the Dangardzong fault. These paths record rapid cooling from ~22 Ma to ~13 Ma, followed by a decrease in cooling rates at ~13-8 Ma and again at ~5 Ma. The changes in cooling rates are interpreted to correspond with a decrease in E-W extension in the Thakkhola graben at these times, related to the initiation of E-W extensional structures elsewhere in the orogen and the partitioning of strain away from the Thakkhola.

6. Acknowledgements

This work was enabled by an NSERC Canada Graduate Scholarship to A. Brubacher, an NSERC Discovery Grant, Accelerator Supplement and Canadian Foundation for Innovation Award to K. Larson. It was further supported by a National Science Foundation grant, NSF-EAR-1119380, awarded to J. Cottle. Apatite and zircon thermochronometry was performed at the Centre for Pure and Applied Tectonics and Thermochronology, which is funded by the Canadian Foundation for Innovation (CFI project 30696). I. Lither aided in the field. P. Tamang, S. Adhikari, the D.G. of the Department of Mines and Geology and the parliamentary office of S. Fuhr are all thanked for their logistical support. Constructive reviews from two anonymous reviews helped better focus this work. Data and Supporting Information can be downloaded here: https://doi.org/10.5683/SP2/ZPSDIT.

7. Figure Captions

Figure 1: A) Map of south Asia, showing N-S compression-related faults (blue) and active E-W extension-related faults (black), modified from Styron et al. (2011) and Yin (2006). Digital elevation data provided by and copyright © of the Japan Aerospace Exploration Agency (JAXA) and used under license therefrom. Warmer colors indicate higher elevations. B) Geology of the Upper Mustang region, based on Hurtado (2002), showing major lithologies and sampling locations from this study. Background digital elevation data is used under license form, and copyright © of JAXA.

Figure 2: Sampling locations and respective U-Th/Pb, $^{40}Ar/^{39}Ar$, and U-Th/He dates (in Ma) for each location. Map modified from Hurtado (2002). Inset depicts an enlarged view of the Ghar

Gompa area with granite sampling locations and structural measurements taken from mica schist. Simplified vertical geological section shown below along line A-B as depicted in the map. Details about the different types of ages are discussed in the text. Symbol shapes represent sampling location: triangle for Ghami, squares for Ghar Gompa, and stars for Dhanggna Khola. Symbol colouring is unique to each specimen and consistent throughout this document. Background imagery is the intellectual property of Esri and is used herein under license. Copyright © 2018 Esri and its licensors. All rights reserved.

Figure 3 - A) Outcrop at the Ghami location, showing leucogranitic Mugu sills/dikes cross-cutting the bedding of the TSS (red dashed lines). B) Outcrop at the Ghar Gompa location showing intrusive contact between the fine-grained granitic Mugu batholith and unmetamorphosed TSS. Red dashed lines outline the trace of bedding in the TSS. C) Outcrop at the Dhanggna Khola location, showing two fine-grained leucogranite dikes horizontally cross cutting both a larger coarse-grained granite vertical dike, and badly weathered granitic orthogneiss. Hammer is approximately 30 cm long.

Figure 4 – Quartz, alkali-feldspar, plagioclase feldspar (QAP) classification diagram for representative specimens from the sites investigated in this work. Photomicrographs of specimens from each site. See text for discussion.

Figure 5 - U-Th/Pb monazite dates from Ghami (A), Ghar Gompa (B-D), and Dhanngna Khola (E-G). Interpreted minimum crystallization age in inset. Weighted mean calculations performed in IsoplotR (Vermeesch, 2018).

Figure 6 - A) ^{40}Ar/^{39}Ar age spectra diagram for Ghami location. B)^{40}Ar/^{39}Ar age spectra diagrams for Ghar Gompa site. C) ^{40}Ar/^{39}Ar age spectra diagrams for Dhanggna Khola site. Symbols correspond to locations on Fig. 2.

Figure 7 - Logratio plots showing zircon and apatite (U-Th)/He ages (Vermeesch, 2008). A) Ghami zircon ages, B) Ghar Gompa zirco ages, C) Ghar Gompa apatite ages, D) Dhanggna Khola zirco ages, E) Dhanggna Khola apatite ages. Preferred ages shown in bold. Number labels correspond to Mineral Analysis # in Table 3.

Figure 8 – Cooling paths calculated for specimens from the sites investigated in this work (as marked). Existing information on the timing of ongoing graben formation is shown above for comparison.

Figure 9 - Summary of cooling paths estimated from this study and the progressive development of E-W extensional structures in the Himalaya-Tibet system through time. Study area is indicated by the star. Left: weighted mean cooling paths for the three field locations from this study, with time period of interest highlighted in red. Right: map of the Himalaya and Tibetan plateau (modified after Styron et al., 2011) indicating E-W extensional structures active in different time periods (red lines). Abbreviations: AD - Ama Drime massif, GB - Gyirong basin, GM - Gurla Mandhata dome, LP - Leo Pagril dome, LU - Lunggar rift, SH - Shuang Hu graben, TG - Thakkhola graben, TY - Tangra-Yumco rift, XD - Xainza-Dinggye rift, YC - Yadong Cross structure, YG - Yadong-Gulu rift.

8. References

Andersen, T. B., & Jamtveit, B. (1990). Uplift of deep crust during orogenic extensional collapse: A model based on field studies in the Sogn-Sunnfjord Region of western Norway. *Tectonics*, *9*(5), 1097–1111.

Armijo, R., Tapponnier, P., Mercier, J. L., & Han, T.-L. (1986). Quaternary extension in southern Tibet: Field observations and tectonic implications. *Journal of Geophysical Research*, *91*(B14), 13803.

Ayres, M., & Harris, N. (1997). REE fractionation and Nd-isotope disequilibrium during crustal anatexis: constraints from Himalayan leucogranites. *Chemical Geology*, *139*(1), 249–269.

Clark, M. K., & Royden, L. H. (2000). Topographic ooze: Building the eastern margin of Tibet by lower crustal flow. *Geology*, *28*(8), 703–706.

Clift, P. D., Hodges, K. V., Heslop, D., Hannigan, R., Van Long, H., & Calves, G. (2008). Correlation of Himalayan exhumation rates and Asian monsoon intensity. *Nature Geoscience*, *1*, 875.

Climate-Data.org. (2019, June 14). Retrieved June 14, 2019, from https://en.climate-data.org/asia/nepal/western-development-region/lo-manthang-53259/

Colchen, M. (1999). The Thakkhola–Mustang graben in Nepal and the late Cenozoic extension in the Higher Himalayas. *Journal of Asian Earth Sciences*, *17*(5–6), 683–702.

Coleman, M., & Hodges, K. (1995). Evidence for Tibetan plateau uplift before 14 Myr ago from a new minimum age for east--west extension. *Nature*, *374*(6517), 49–52.

Constenius, K. N. (1996). Late Paleogene extensional collapse of the Cordilleran foreland fold and thrust belt. *GSA Bulletin*, *108*(1), 20–39.

Cooper, F. J., Hodges, K. V., Parrish, R. R., Roberts, N. M. W., & Horstwood, M. S. A. (2015). Synchronous N-S and E-W extension at the Tibet-to-Himalaya transition in NW Bhutan. *Tectonics*, *34*(7), 2014TC003712.

Copeland, P., Harrison, T. M., & Le Fort, P. (1990). Age and cooling history of the Manaslu granite: implications for Himalayan tectonics. *Journal of Volcanology and Geothermal Research*, *44*(33–50).

Cottle, J. M., Jessup, M. J., Newell, D. L., Horstwood, M. S. A., Noble, S. R., Parrish, R. R., et al. (2009). Geochronology of granulitized eclogite from the Ama Drime Massif: Implications for the tectonic evolution of the South Tibetan Himalaya. *Tectonics*, *28*, TC1002.

Cottle, J. M., Kylander-Clark, A. R., & Vrijmoed, J. C. (2012). U–Th/Pb geochronology of detrital zircon and monazite by single shot laser ablation inductively coupled plasma mass spectrometry (SS-LA-ICPMS). *Chemical Geology*, *332–333*, 136–147.

Deniel, C., Vidal, P., Fernandez, A., Le Fort, P., & Peucat, J.-J. (1987). Isotopic study of the Manaslu granite (Himalaya, Nepal): inferences on the age and source of Himalayan leucogranites. *Contributions to Mineralogy and Petrology. Beitrage Zur Mineralogie Und Petrologie*, *96*(1), 78–92.

Dewane, T. J., Stockli, D. F., Hager, C., Taylor, M., Ding, L., Lee, J., & Wallis, S. (2006). Timing of Cenozoic EW extension in the Tangra Yum Co-Kung Co Rift, south-central Tibet. In *AGU Fall Meeting Abstracts*. adsabs.harvard.edu. Retrieved from http://adsabs.harvard.edu/abs/2006AGUFM.T34C..04D

Dewey, J. F. (1988). Extensional collapse of orogens. *Tectonics*, *7*(6), 1123–1139.

Dodson, M. (1973). Closure temperature in cooling geochronological and petrological systems. *Contributions to Mineralogy and Petrology*, *40*, 259–274.

Fitzgerald, P. G., Baldwin, S. L., Webb, L. E., & O'Sullivan, P. B. (2006). Interpretation of (U–Th)/He single grain ages from slowly cooled crustal terranes: A case study from the Transantarctic Mountains of southern Victoria Land. *Chemical Geology*, *225*(1–2), 91–120.

Flowers, R. M., Ketcham, R. A., Shuster, D. L., & Farley, K. A. (2009). Apatite (U–Th)/He thermochronometry using a radiation damage accumulation and annealing model. *Geochimica et Cosmochimica Acta*, *73*(8), 2347–2365.

Fort, M., Bassoullet, J. P., Colchen, M., & Freytet, P. (1981). Sedimentological and structural evolution of the Thakkhola-Mustang graben (Nepal Himalaya) during late Neogene and Pleistocene. In *Proceedings* (pp. 25–35). India: Geological Survey of India.

Fort, M., Freytet, P., & Colchen, M. (1982). Structural and sedimentological evolution of the Thakkhola Mustang graben (Nepal Himalayas). *Zeitschrift Für Geomorphologie*, *42*, 75–98.

Fu, J., Li, G., Wang, G., Zhang, L., Liang, W., Zhang, Z., et al. (2018). Synchronous granite intrusion and E–W extension in the Cuonadong dome, southern Tibet, China: evidence from field observations and thermochronologic results. *International Journal of Earth Sciences*, 1–19.

Garzione, C. N., Dettman, D. L., Quade, J., DeCelles, P. G., & Butler, R. F. (2000). High times on the Tibetan Plateau: Paleoelevation of the Thakkhola graben, Nepal. *Geology*, *28*(4), 339–342.

Garzione, C. N., DeCelles, P. G., Hodkinson, D. G., Ojha, T. P., & Upreti, B. N. (2003). East-west extension and Miocene environmental change in the southern Tibetan plateau: Thakkhola graben, central Nepal. *Geological Society of America Bulletin*, *115*(1), 3–20.

Gehrels, G. E., DeCelles, P. G., Ojha, T. P., & Upreti, B. N. (2006a). Geologic and U–Pb geochronologic evidence for early Paleozoic tectonism in the Dadeldhura thrust sheet, far-west Nepal Himalaya. *Journal of Asian Earth Sciences*, *28*(4–6), 385–408.

Gehrels, G. E., DeCelles, P. G., Ojha, T. P., & Upreti, B. N. (2006b). Geologic and U-Th-Pb geochronologic evidence for early Paleozoic tectonism in the Kathmandu thrust sheet, central Nepal Himalaya. *Geological Society of America Bulletin*, *118*(1–2), 185–198.

Godin, L., Parrish, R. R., Brown, R. L., & Hodges, K. V. (2001). Crustal thickening leading to exhumation of the Himalayan Metamorphic core of central Nepal: Insight from U-Pb Geochronology and ^{40}Ar/^{39}Ar Thermochronology. *Tectonics*, *20*(5), 729–747.

Grove, M., & Harrison, T. M. (1996). ^{40}Ar* diffusion in Fe-rich biotite. *The American Mineralogist*, *81*, 940–951.

Guenthner, W. R., Reiners, P. W., Ketcham, R. A., Nasdala, L., & Giester, G. (2013). Helium diffusion in natural zircon: Radiation damage, anisotropy, and the interpretation of zircon (U-Th)/He thermochronology. *American Journal of Science*, *313*(3), 145–198.

Guillot, S., Pecher, A., & Le Fort, P. (1995). Tectonic and thermal constraints on emplacement of Himalayan leucogranites. *C.R. Acad. Sci. Paris*, *320*, 55–61.

Harrison, T. M., Lovera, O. M., & Grove, M. (1997). New insights into the origin of two contrasting Himalayan granite belts. *Geology*, *25*(10), 899–902.

Harrison, T. M., Célérier, J., Aikman, A. B., Hermann, J., & Heizler, M. T. (2009). Diffusion of ^{40}Ar in muscovite. *Geochimica et Cosmochimica Acta*, *73*(4), 1039–1051.

Hodges, K. V. (2000). Tectonics of the Himalaya and southern Tibet from two perspectives. *Geological Society of America Bulletin*, *112*(3), 324–350.

Hurtado, J. M. (2002). *Tectonic Evolution of the Thakkhola Graben and Dhaulagiri Himalaya, Central Nepal* (PhD). Massachusetts Institute of Technology.

Hurtado, J. M., Hodges, K. V., & Whipple, K. (2001). Neotectonics of the Thakkhola graben and implications for recent activity on the South Tibetan fault system in the central Nepal Himalaya. *Geological Society of America Bulletin*, *113*(2), 222–240.

Jessup, M. J., Newell, D. L., Cottle, J. M., Berger, A. L., & Spotila, J. A. (2008). Orogen-parallel extension and exhumation enhanced by denudation in the trans-Himalayan Arun River gorge, Ama Drime Massif, Tibet-Nepal. *Geology*, *36*(7), 587.

Kali, E., Leloup, P., Arnaud, N., Mahéo, G., Liu, D., Boutonnet, E., et al. (2010). Exhumation history of the deepest central Himalayan rocks, Ama Drime range: Key pressure-temperature-deformation-time constraints on orogenic models. *Tectonics*, *29*(2), 1–31.

Ketcham, R. A. (2005). Forward and Inverse Modeling of Low-Temperature Thermochronometry Data. *Reviews in Mineralogy and Geochemistry*, *58*(1), 275–314.

Kirby, E., Reiners, P. W., Krol, M. A., Whipple, K. X., Hodges, K. V., Farley, K. A., et al. (2002). Late Cenozoic evolution of the eastern margin of the Tibetan Plateau: Inferences from ^{40}Ar/^{39}Ar and (U-Th)/He thermochronology. *Tectonics*, *21*(1), 1-1-1–20.

Lanphere, M. A., & Dalrymple, B. G. (1976). Identification of excess ^{40}Ar by the ^{40}Ar/^{39}Ar age spectrum technique. *Earth and Planetary Science Letters*, *32*(2), 141–148.

Larson, K. P., Camacho, A., Cottle, J. M., Coutand, I., Buckingham, H. M., Ambrose, T. K., & Rai, S. M. (2017). Cooling, exhumation, and kinematics of the Kanchenjunga Himal, far east Nepal: Exhumation of the Kanchenjunga Himal. *Tectonics*, *36*(6), 1037–1052.

Larson, K. P., Kellett, D. A., Cottle, J. M., Camacho, A., & Brubacher, A. D. (2019). Mid-Miocene initiation of E-W extension and recoupling of the Himalaya. *Terra Nova*, *42*, 75.

Le Fort, P., & France-Lanord, C. (1994). Granites from Mustang and surrounding regions, central Nepal. *Journal of Nepal Geological Society*, *10*, 79–81.

Le Fort, P., Cuney, M., Deniel, C., France-Lanord, C., Sheppard, S. M., Upreti, B. N., & Vidal, P. (1987). Crustal generation of the Himalayan leucogranites. *Tectonophysics*, *134*(39–57).

Lederer, G. W., Cottle, J. M., Jessup, M. J., Langille, J. M., & Ahmad, T. (2013). Timescales of partial melting in the Himalayan middle crust: insight from the Leo Pargil dome, northwest India. *Contributions to Mineralogy and Petrology. Beitrage Zur Mineralogie Und Petrologie*, *166*, 1415–1441.

Leloup, P., Mahéo, G., Arnaud, N., & Kali, E. (2010). The South Tibet detachment shear zone in the Dinggye area: Time constraints on extrusion models of the Himalayas. *Earth and Planetary Science Letters*, *292*(1–2), 1–16.

Lihter, I., Larson, K. P., Shrestha, S., Cottle, J. M., & Brubacher, A. D. (2020). Contact metamorphism of the Tethyan Sedimentary Sequence, Upper Mustang region, west-central Nepal. *Geological Magazine*, *GEO-19-2362R*.

Meesters, A. G. C. A., & Dunai, T. J. (2002). Solving the production–diffusion equation for finite diffusion domains of various shapes. *Chemical Geology*, *186*(3–4), 333–344.

Meigs, A., Burbank, D., & Beck. (1995). Middle-late Miocene (> 10 Ma) formation of the Main Boundary thrust in the western Himalaya. *Geology*, *23*(5), 423–426.

Mitsuishi, M., Wallis, S. R., Aoya, M., & Lee, J. (2012). E–W extension at 19 Ma in the Kung Co area, S. Tibet: Evidence for contemporaneous E–W and N–S extension in the

Himalayan orogen. *Earth and Planetary Science Letters*, *325–326*, 10–20.

Molnar, P., & Stock, J. M. (2009). Slowing of India's convergence with Eurasia since 20 Ma and its implications for Tibetan mantle dynamics. *Tectonics*, *28*(3), TC3001.

Murphy, M. A., & Copeland, P. (2005). Transtensional deformation in the central Himalaya and its role in accommodating growth of the Himalayan orogen: Transtension in the Himalaya. *Tectonics*, *24*(4). https://doi.org/10.1029/2004TC001659

Platt, J. P., & Vissers, R. L. M. (1989). Extensional collapse of thickened continental lithosphere: A working hypothesis for the Alboran Sea and Gibraltar arc. *Geology*, *17*(6), 540–543.

Ratschbacher, L., Krumrei, I., Blumenwitz, M., Staiger, M., Gloaguen, R., Miller, B. V., et al. (2011). Rifting and strike-slip shear in central Tibet and the geometry, age and kinematics of upper crustal extension in Tibet. *Geological Society, London, Special Publications*, *353*(1), 127–163.

Replumaz, A., Negredo, A. M., Villasenor, A., & Guillot, S. (2010). Indian continental subduction and slab break-off during Tertiary collision. *Terra Nova*, *22*(4), 290–296.

Schärer, U. (1984). The effect of initial ^{230}Th disequilibrium on young U-Pb ages: the Makalu case, Himalaya. *Earth and Planetary Science Letters*, *67*, 191–204.

Searle, M. P., Cottle, J. M., Streule, M. J., & Waters, D. J. (2010). Crustal melt granites and migmatites along the Himalaya: melt source, segregation, transport and granite emplacement mechanisms. *Earth and Environmental Science Transactions of the Royal Society of Edinburgh*, *100*, 219–233.

Shuster, D. L., Flowers, R. M., & Farley, K. A. (2006). The influence of natural radiation damage on helium diffusion kinetics in apatite. *Earth and Planetary Science Letters*, *249*(3), 148–161.

Styron, R. H., Taylor, M. H., & Murphy, M. A. (2011). Oblique convergence, arc-parallel extension, and the role of strike-slip faulting in the High Himalaya. *Geosphere, 7*(2), 582–596.

Sun, X., & Wang, P. (2005). How old is the Asian monsoon system?—Palaeobotanical records from China. *Palaeogeography, Palaeoclimatology, Palaeoecology, 222*(3), 181–222.

Teng, L. S. (1996). Extensional collapse of the northern Taiwan mountain belt. *Geology*, *24*(10), 949–952.

Thiede, R. C., Arrowsmith, R., Bookhagen, B., McWilliams, M., Sobel, E. R., & Strecker, M. R. (2006). Dome formation and extension in the Tethyan Himalaya, Leo Pargil, northwest India. *Geological Society of America Bulletin, 118*(5/6), 635–650.

Vermeesch, P. (2008). Three new ways to calculate average (U–Th)/He ages. *Chemical Geology, 249*(3), 339–347.

Vermeesch, P. (2010). HelioPlot, and the treatment of overdispersed (U–Th–Sm)/He data. *Chemical Geology*, *271*(3), 108–111.

Vermeesch, P. (2018). IsoplotR: A free and open toolbox for geochronology. *Geoscience Frontiers*, *9*(5), 1479–1493.

Visonà, D., & Lombardo, B. (2002). Two-mica and tourmaline leucogranites from the Everest–Makalu region (Nepal–Tibet). Himalayan leucogranite genesis by isobaric heating? *Lithos*, *62*(3–4), 125–150.

Yin, A. (2006). Cenozoic tectonic evolution of the Himalayan orogen as constrained by along-strike variation of structural geometry, exhumation history, and foreland sedimentation. *Earth Science Reviews*, *76*, 1–131.

Yin, A., & Harrison, T. M. (2000). Geologic evolution of the Himalayan-Tibetan orogen. *Annual*

Review of Earth and Planetary Sciences, *28*, 211–280.
Yin, A., Kapp, P. A., Murphy, M. A., Manning, C. E., Mark Harrison, T., Grove, M., et al. (1999). Significant late Neogene east-west extension in northern Tibet. *Geology*, *27*(9), 787–790.

Carrapa, B., Orme, D. A., DeCelles, P. G., Kapp, P., Cosca, M. A., & Waldrip, R. (2014). Miocene burial and exhumation of the India-Asia collision zone in southern Tibet: Response to slab dynamics and erosion. *Geology*. https://doi.org/10.1130/g35350.1
Cherniak, D. J., Watson, E. B., & Thomas, J. B. (2009). Diffusion of helium in zircon and apatite. *Chemical Geology*, *268*(1), 155–166.
Copeland, P., Mark Harrison, T., Pan, Y., Kidd, W. S. F., Roden, M., & Zhang, Y. (1995). Thermal evolution of the Gangdese batholith, southern Tibet: A history of episodic unroofing. *Tectonics*. https://doi.org/10.1029/94tc01676
Dai, J., Wang, C., Hourigan, J., Li, Z., & Zhuang, G. (2013). Exhumation History of the Gangdese Batholith, Southern Tibetan Plateau: Evidence from Apatite and Zircon (U-Th)/He Thermochronology. *The Journal of Geology*, *121*(2), 155–172.
Dodson, M. (1973). Closure temperature in cooling geochronological and petrological systems. *Contributions to Mineralogy and Petrology*, *40*, 259–274.
Hurtado, J. M. (2002). *Tectonic Evolution of the Thakkhola Graben and Dhaulagiri Himalaya, Central Nepal* (PhD). Massachusetts Institute of Technology.
Jaeger, J. C. (1964). Thermal effects of intrusions. *Reviews of Geophysics* , *2*(3), 443.
Jaeger, J. C. (1968). Cooling and solidification of igneous rocks. In H. H. Hess & A. Poldervaart (Eds.), *Basalts, the Poldervaart treatise on rocks of basaltic composition* (Vol. 2, pp.

503–536). New York-London-Sidney: Wiley.

Larson, K. P., Kellett, D. A., Cottle, J. M., Camacho, A., & Brubacher, A. D. (2019). Mid-Miocene initiation of E-W extension and recoupling of the Himalaya. *Terra Nova*, *42*, 75.

Lihter, I., Larson, K. P., Shrestha, S., Cottle, J. M., & Brubacher, A. D. (2020). Contact metamorphism of the Tethyan Sedimentary Sequence, Upper Mustang region, west-central Nepal. *Geological Magazine, GEO-19-2362R*.

Nabelek, P. I., Hofmeister, A. M., & Whittington, A. G. (2012). The influence of temperature-dependent thermal diffusivity on the conductive cooling rates of plutons and temperature-time paths in contact aureoles. *Earth and Planetary Science Letters*, *317–318*, 157–164.

Shen, T., Wang, G., Leloup, P. H., van der Beek, P., Bernet, M., Cao, K., et al. (2016). Controls on Cenozoic exhumation of the Tethyan Himalaya from fission-track thermochronology and detrital zircon U-Pb geochronology in the Gyirong basin area, southern Tibet: The Tethyan Himalaya Cenozoic Exhumation. *Tectonics*, *35*(7), 1713–1734.

Whittington, A. G., Hofmeister, A. M., & Nabelek, P. I. (2009). Temperature-dependent thermal diffusivity of the Earth's crust and implications for magmatism. *Nature*, *458*(7236), 319–321.

Cottle, J. M., Jessup, M. J., Newell, D. L., Horstwood, M. S. A., Noble, S. R., Parrish, R. R., et al. (2009). Geochronology of granulitized eclogite from the Ama Drime Massif: Implications for the tectonic evolution of the South Tibetan Himalaya. *Tectonics*, *28*, TC1002.

Hurtado, J. M. (2002). *Tectonic Evolution of the Thakkhola Graben and Dhaulagiri Himalaya, Central Nepal* (PhD). Massachusetts Institute of Technology.

Jessup, M. J., Newell, D. L., Cottle, J. M., Berger, A. L., & Spotila, J. A. (2008). Orogen-parallel extension and exhumation enhanced by denudation in the trans-Himalayan Arun River gorge, Ama Drime Massif, Tibet-Nepal. *Geology*, *36*(7), 587.

Larson, K. P., Kellett, D. A., Cottle, J. M., Camacho, A., & Brubacher, A. D. (2019). Mid-Miocene initiation of E-W extension and recoupling of the Himalaya. *Terra Nova*, *42*, 75.

Figure 1.

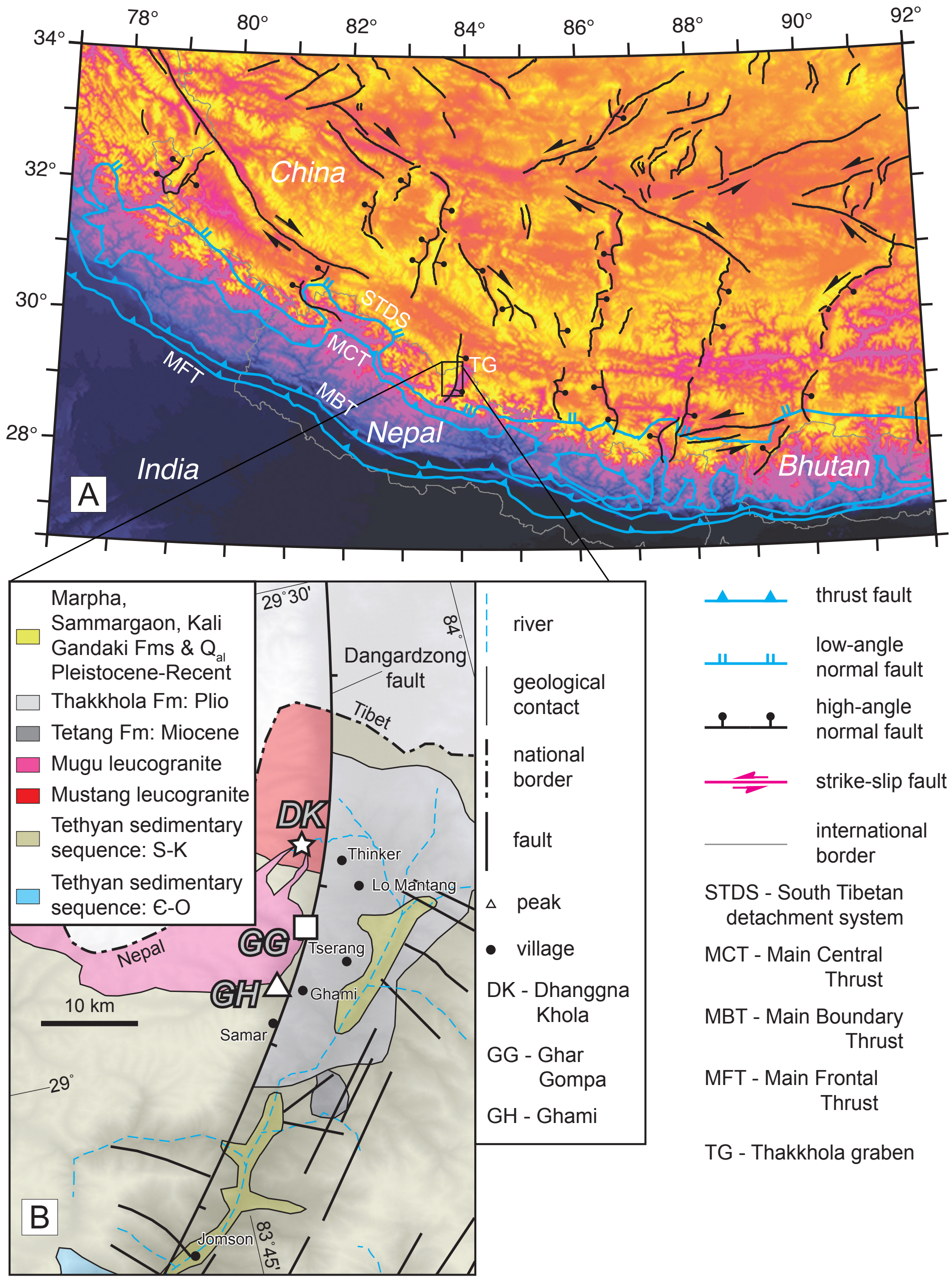

Brubacher et al. Figure 1

Figure 2.

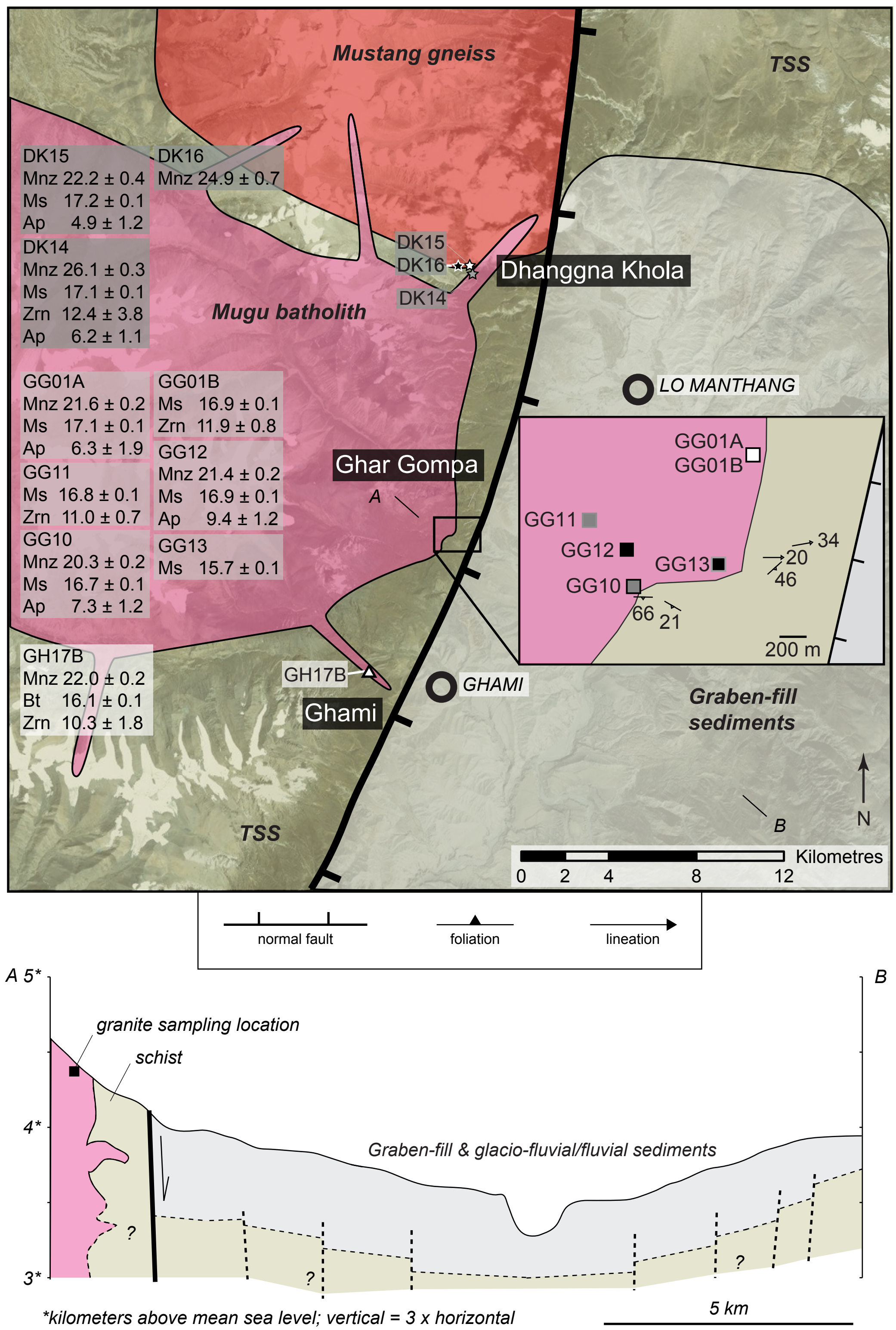

Brubacher et al. Figure 2

Figure 3.

Brubacher et al. Figure 3

Figure 4.

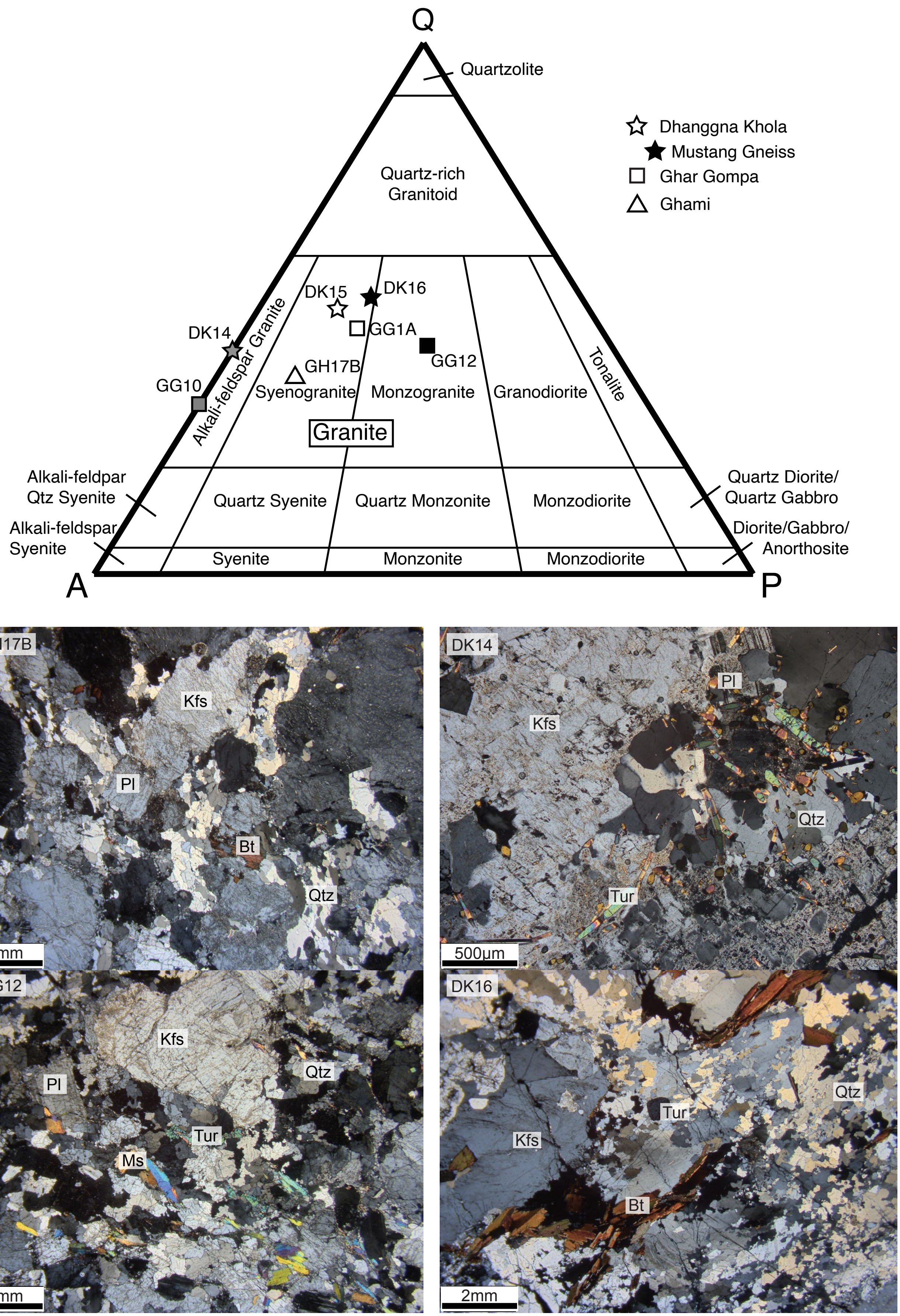

Brubacher et al. Figure 4

Figure 5.

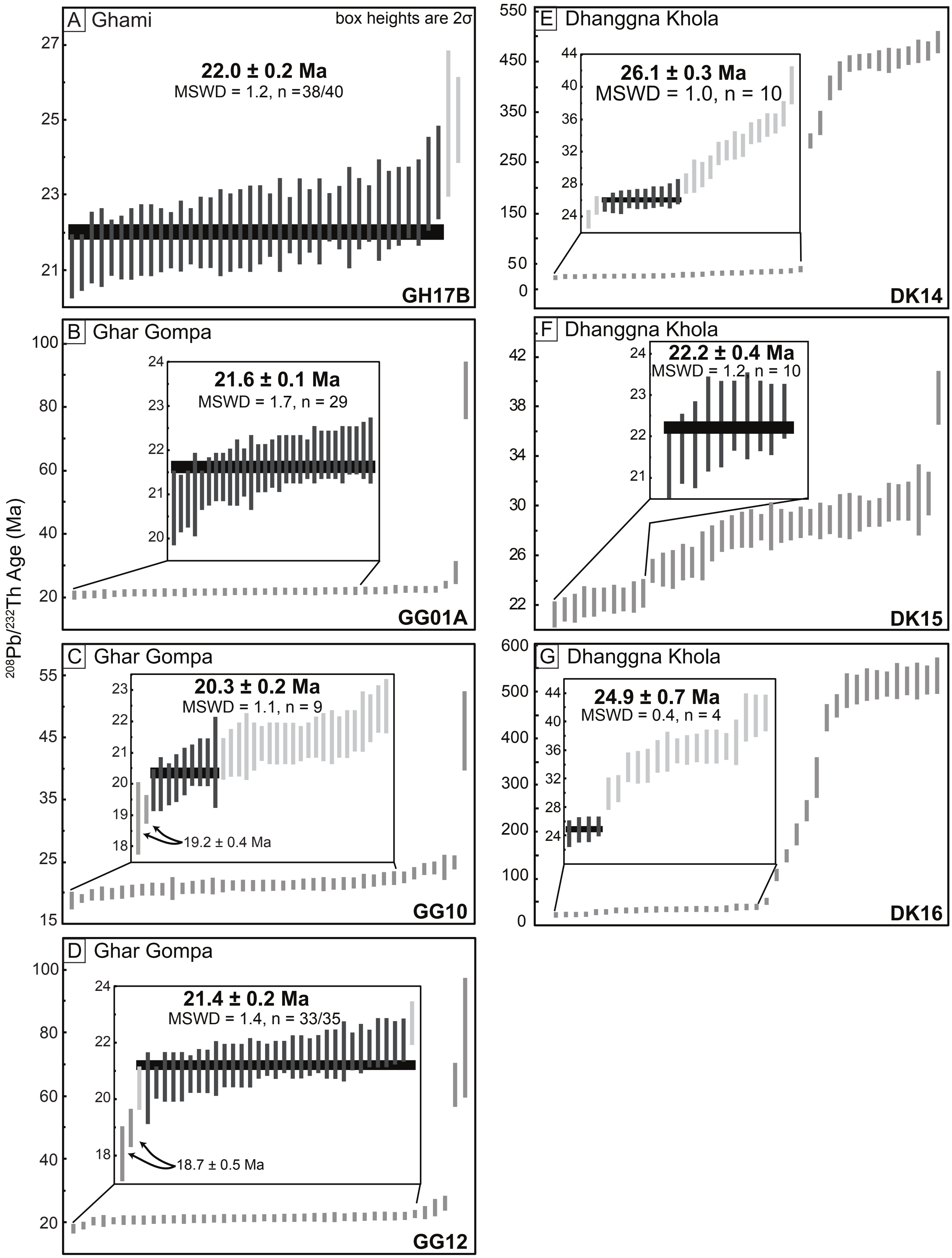

Brubacher et al. Figure 5

Figure 6.

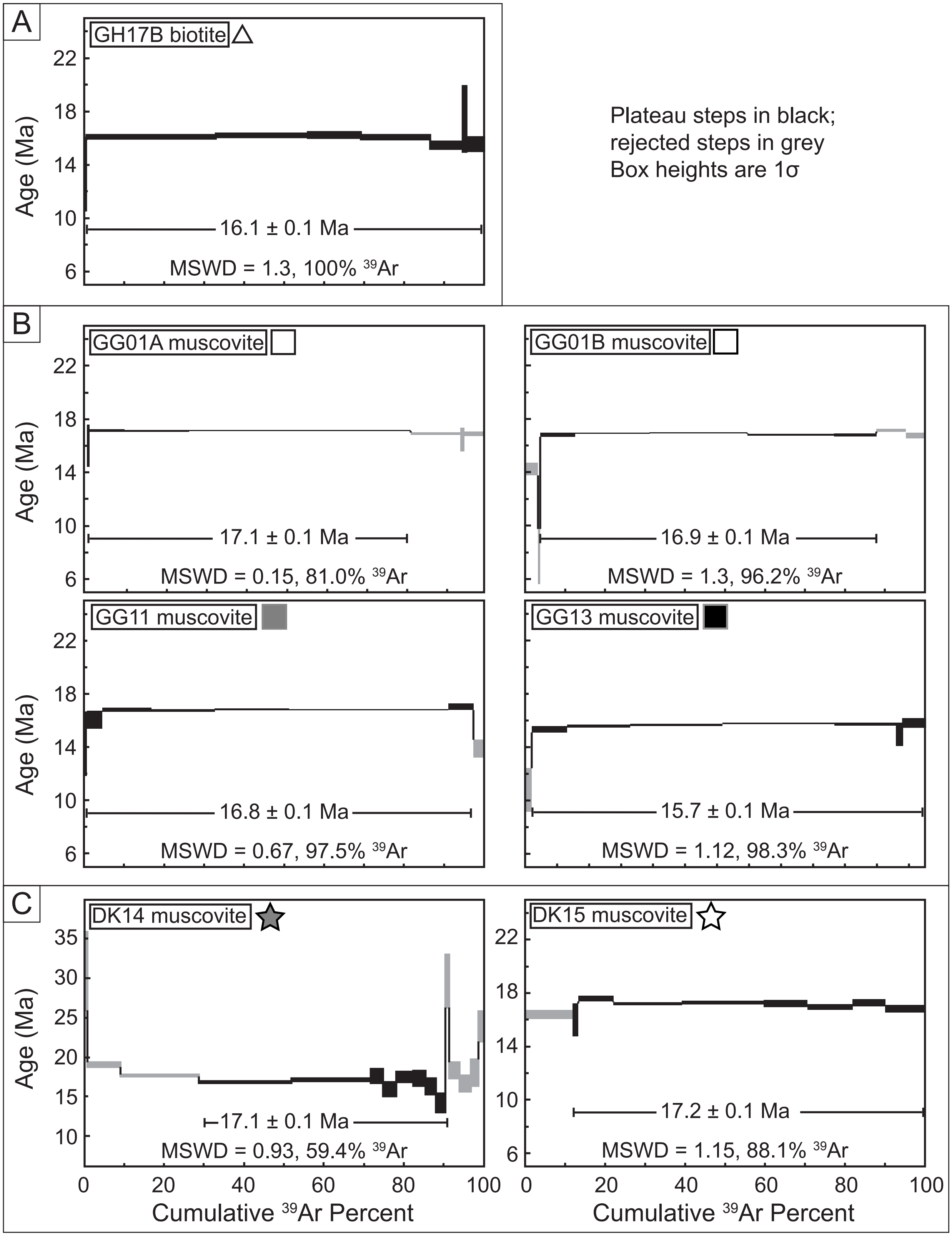

Brubacher et al. Figure 6

Figure 7.

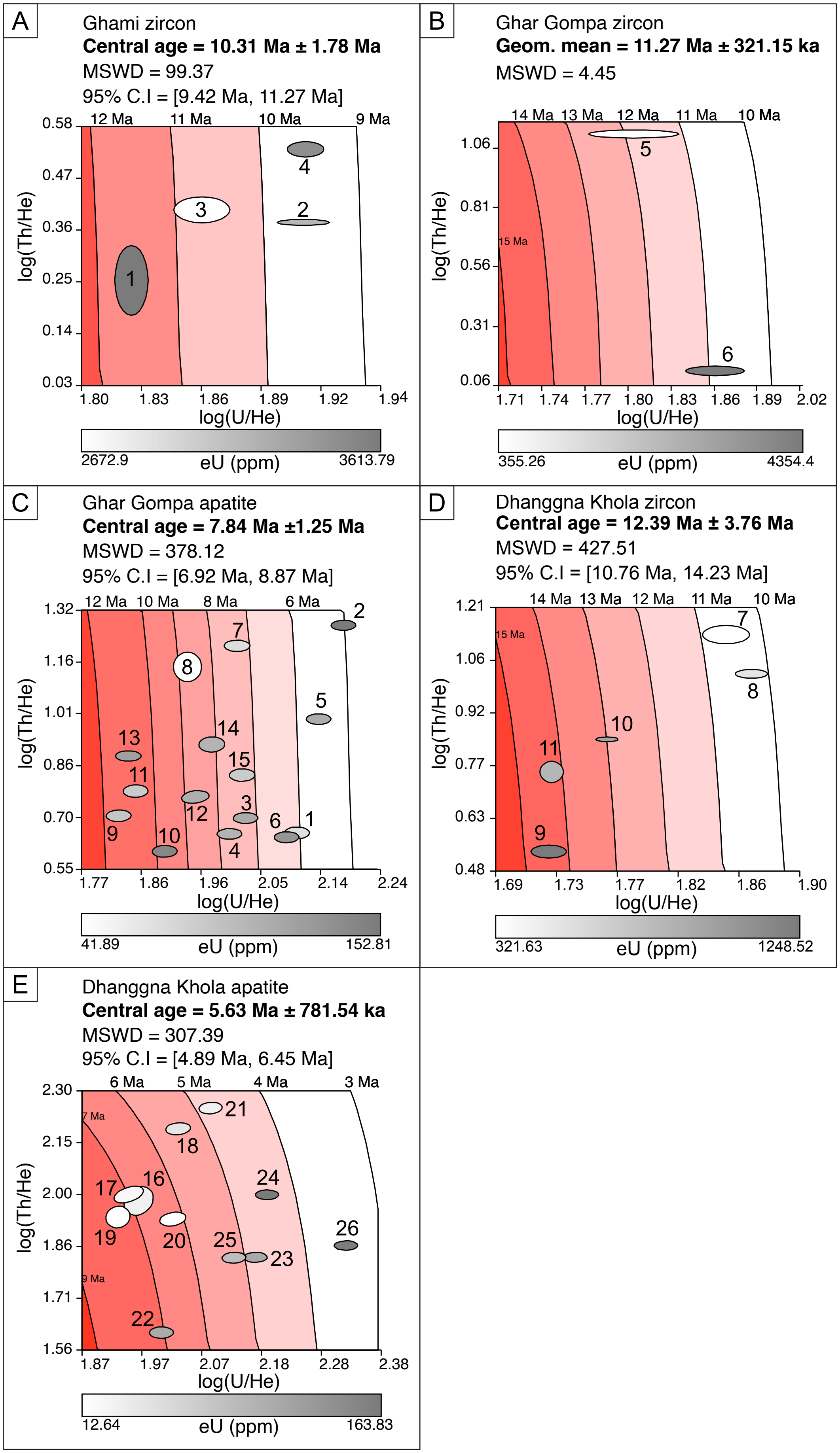

Brubacher et al. Figure 7

Figure 8.

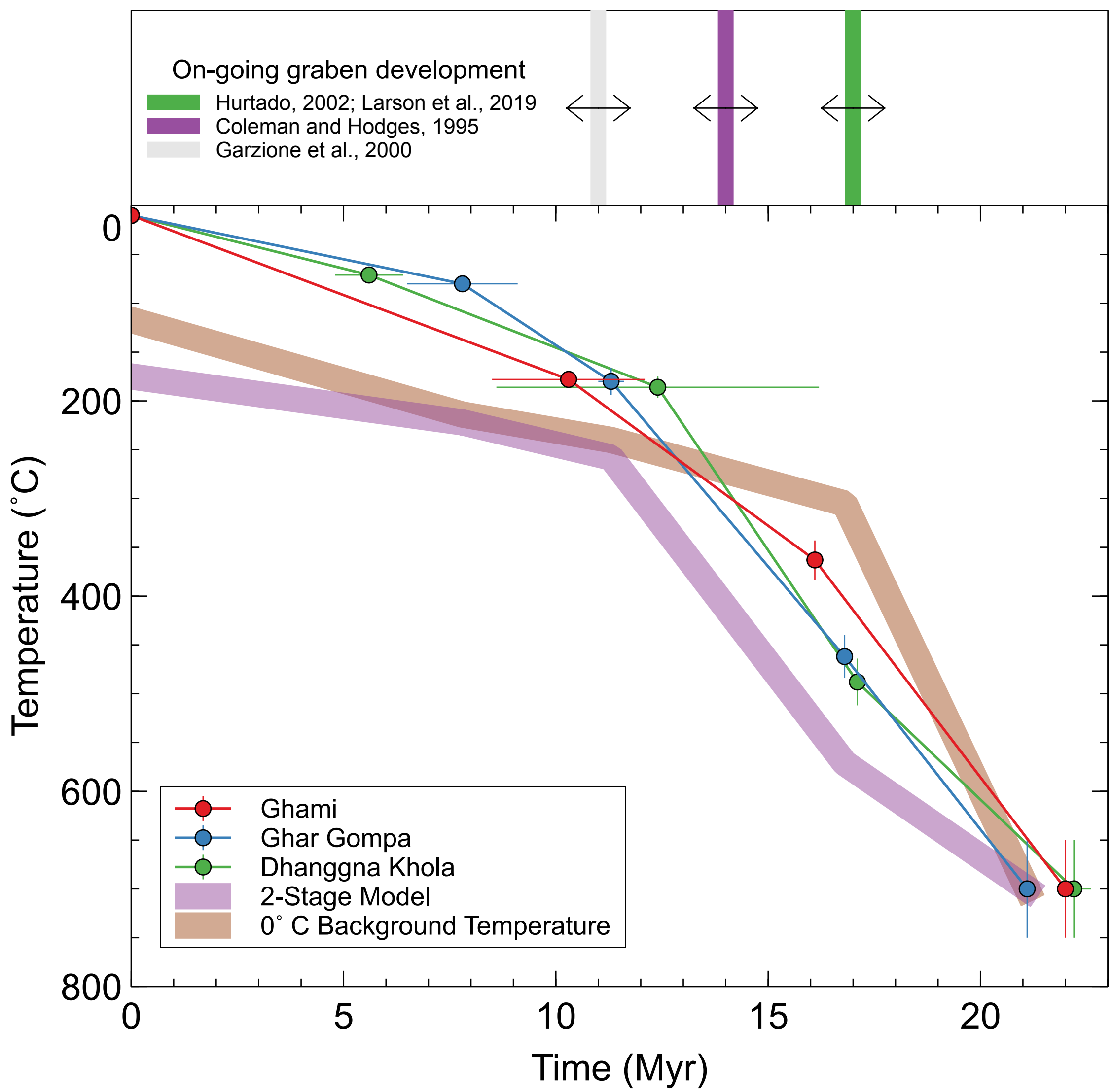

Brubacher et al. Figure 8

Figure 9.

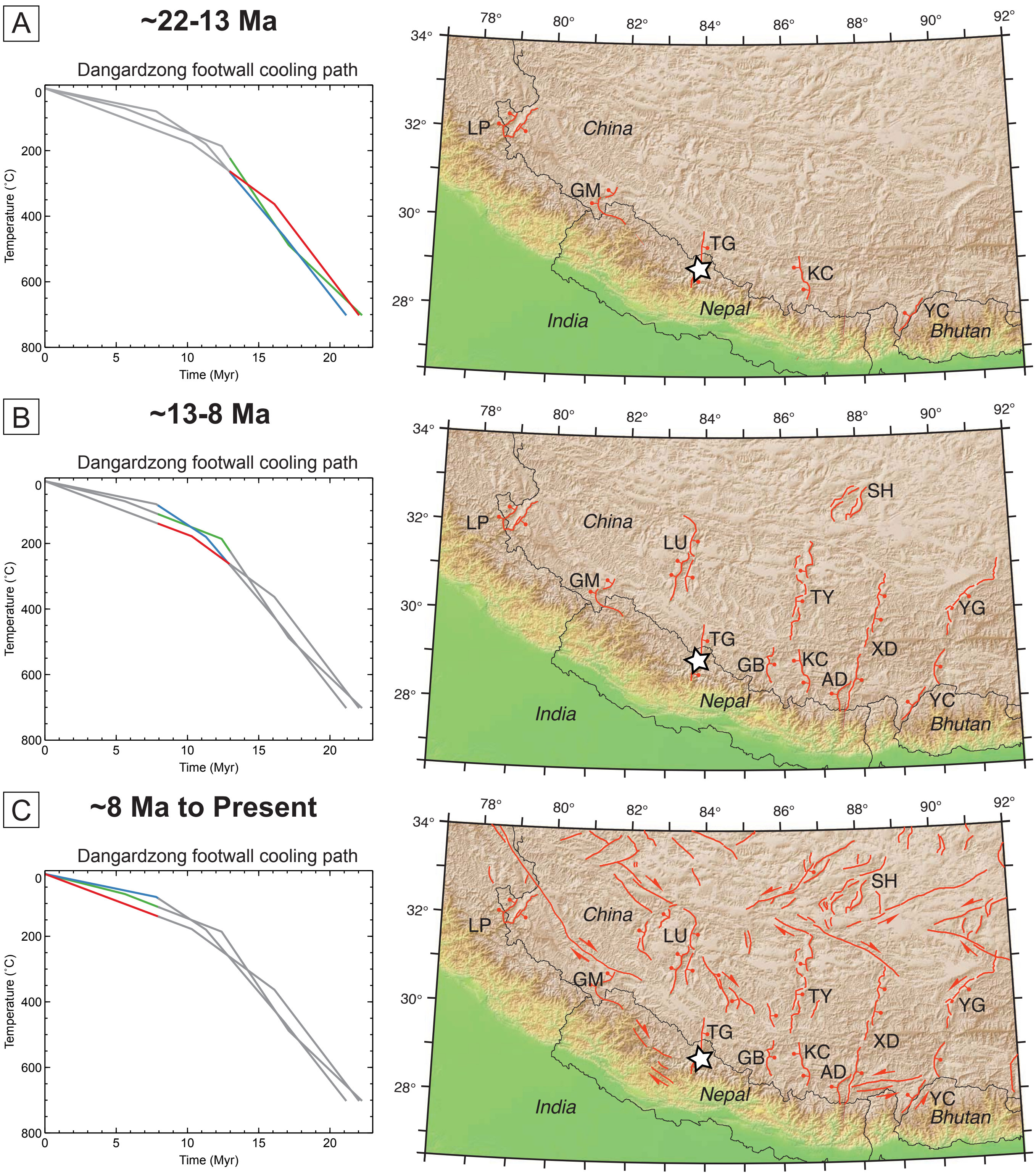

Brubacher et al. Figure 9

Table 1. Mineralogy and lithology of specimens investigated

Location	Specimen	Mineral Assemblage†	Lithology
Ghami	GH17B	Qz + Kfs + Pl + Bt	granite
Ghar Ghompa	GG01A	Qz + Kfs + Pl + Ms + Bt	granite
	GG01B	Qz + Kfs + Pl + Ms + Tur ± Bt ± Grt	granite
	GG10	Qz + Kfs + Pl + Ms + Tur ± Grt	alkali-feldspar granite
	GG11	Qz + Kfs + Pl + Ms + Tur ± Bt ± Grt	granite
	GG12	Qz + Kfs + Pl + Ms + Tur	granite
	GG13	Qz + Kfs + Pl + Ms + Tur ± Bt ± Grt	granite
Dhanggna Khola	DK14	Qz + Kfs + Pl + Ms + Tur	alkali-feldspar granite
	DK15	Qz + Kfs + Pl + Ms + Tur	leucogranite dyke
	DK16	Qz + Kfs + Pl + Bt + Ms	granitic orthogneiss with Kfs augen

†Abbreviations after Whitney and Evans (2010).

Table 2. $^{40}Ar/^{39}Ar$ geochronology result summary

Location	Specimen	Mineral	Plateau Age (Ma)	± 2σ	Tc (°C)	± 2σ	% ^{39}Ar released	MSWD
Ghami	GH17B	Bt	16.1	0.2	363	20	100.0	1.30
Ghar Ghompa	GG01A	Ms	17.1	0.2	507	39	81.0	0.15
	GG01B	Ms	16.9	0.2	477	46	96.2	1.30
	GG10	Ms	16.7	0.2	473	32	100.0	0.96
	GG11	Ms	16.8	0.2	487	32	97.5	0.67
	GG12	Ms	16.9	0.2	498	34	71.2	1.30
	GG13	Ms	15.7	0.2	480	38	98.3	1.12
Dhanggna Khola	DK14	Ms	17.1	0.2	535	45	59.4	0.93
	DK15	Ms	17.2	0.2	475	30	88.1	1.15

Table 3. Zircon and apatite U-Th-He data summary

Location	Mineral Analysis #	Specimen ID	Age (Ma)	±	Total U (ppm)	±	Total Th (ppm)	±	eU (ppm)	eR (μm)	Closure Temperature (˚C)
					Zircon						
Ghami	1	17B-1	11.65	0.72	3591.86	32.81	93.32	8.11	3613.79	49.75	178 ± 9
	2	17B-3	9.65	0.63	3164.88	44.81	90.85	0.68	3186.24	59.84	
	3	**17B-4**	**10.77**	**0.64**	**2651.62**	**40.74**	**90.58**	**2.92**	**2672.90**	**43.03**	
	4	17B-5	9.59	0.61	3444.89	34.33	141.90	2.71	3478.24	56.39	
Ghar Gompa	5	01B-1	11.92	0.77	339.03	11.88	69.10	1.37	355.26	45.55	180 ± 14
	6	**11-3**	**10.97**	**0.70**	**4336.08**	**98.61**	**77.94**	**1.81**	**4354.40**	**50.16**	
Dhanggna Khola	7	14-2	10.65	0.67	308.07	5.74	57.72	1.66	321.63	49.20	186 ± 11
	8	14-3	10.34	0.68	418.26	5.37	58.72	0.79	432.06	64.10	
	9	14-4	14.54	0.88	1230.32	17.39	77.47	1.57	1248.52	46.02	
	10	**14-5**	**13.08**	**0.84**	**829.41**	**7.38**	**96.82**	**0.71**	**852.16**	**57.08**	
	11	14-6	14.33	0.90	704.17	6.56	73.09	2.46	721.35	53.62	
					Apatite						
Ghar Gompa	1	1A-1	6.10	0.10	57.76	1.28	1.99	0.04	58.22	70.95	80 ± 6
	2	1A-2	5.05	0.08	148.60	3.28	17.93	0.30	152.81	67.75	
	3	1A-3	7.32	0.13	98.99	2.19	4.55	0.08	100.06	73.22	
	4	1A-4	7.76	0.14	89.69	1.98	3.92	0.07	90.61	89.55	
	5	1A-5	5.59	0.09	97.55	2.15	6.78	0.12	99.14	66.67	
	6	1A-6	6.33	0.10	120.04	2.65	4.18	0.08	121.02	61.30	
	7	**10-1**	**7.35**	**0.13**	**57.93**	**1.34**	**8.91**	**0.17**	**60.03**	**42.43**	
	8	10-2	8.78	0.16	40.38	1.02	6.43	0.33	41.89	47.78	
	9	12-1	11.48	0.18	75.37	1.67	5.56	0.11	76.68	50.40	
	10	12-3	9.78	0.14	136.12	3.02	6.67	0.13	137.69	40.00	
	11	12-4	10.78	0.16	72.50	1.61	5.96	0.13	73.90	43.94	
	12	12-5	8.73	0.14	94.19	2.10	6.00	0.11	95.60	51.73	
	13	12-7	11.00	0.16	107.03	2.46	11.47	0.20	109.73	37.81	
	14	12-8	8.19	0.14	89.64	2.08	7.70	0.20	91.45	37.07	
	15	12-9	7.38	0.13	71.98	1.67	4.50	0.10	73.04	52.32	
Dhanggna Khola	16	14-1	6.86	0.12	14.31	0.35	14.60	0.64	17.74	39.51	71 ± 6
	17	14-2	7.01	0.12	11.97	0.27	13.22	0.26	15.07	39.93	
	18	14-3	5.46	0.08	16.20	0.37	22.59	0.40	21.51	51.90	
	19	14-4	7.47	0.11	10.24	0.23	10.21	0.35	12.64	48.72	
	20	14-5	6.26	0.10	10.91	0.25	8.62	0.16	12.93	45.62	
	21	14-6	4.80	0.06	13.55	0.30	18.98	0.33	18.01	54.67	
	22	15-1	7.12	0.11	65.19	1.54	25.76	0.48	71.25	36.37	
	23	**15-2**	**4.84**	**0.09**	**65.77**	**1.52**	**29.17**	**0.45**	**72.63**	**44.84**	
	24	15-3	4.44	0.07	142.50	3.28	90.75	1.40	163.83	45.26	
	25	15-4	5.23	0.12	44.38	1.03	21.39	0.36	49.40	42.26	
	26	15-5	3.46	0.05	151.40	3.51	50.59	0.77	163.28	45.56	

Table 4. Timing of E-W structures across Tibet

Location[†]	Age (Ma)	Structure	Rheology	Reference
YC	< 14	Lingshi normal fault	brittle	Cooper et al., 2015
YG	≤ 11.5	Yadong graben	ductile	Ratschbacher et al., 2011
YG	8 ± 1	Nyainqentanghla shear zone	ductile	Harrison et al., 1995
XD	ca. 8-13	Dinggye normal fault	brittle	Zhang and Guo, 2007
AD	≥ 11	Dinggye normal fault	brittle	Leloup et al., 2010
AD	12 ± 1	Dinggye and Kharta shear zones	ductile	Kali et al., 2010
AD	12 ± 1	Nyönno Ri detachment	ductile	Langille et al., 2010
KC	ca. 12-13	Kung Co rift	brittle	Lee et al., 2011
TY	ca. 13	Tangra-Yumco rift	n/a	Dewane et al., 2006
GB	≥ 11	Gyirong basin	brittle	Xu et al., 2012
SH	≥ 13.5	Shuang Hu graben	brittle	Blisniuk et al., 2001
LU	ca. 8	Lunggar Rift	brittle	Styron et al., 2013
YG	ca. 5	Ringbung graben	brittle	Ratschbacher et al., 2011
YG	ca. 5	Nyainqentanghla shear zone	brittle	Harrison et al., 1995
YG	ca. 5-7	Gulu rift	brittle	Stockli et al., 2002
AD	ca. 6-4	Dinggye normal fault	brittle	Kali et al., 2010
TY	ca. 6	Tangra-Yumco rift	brittle	Dewane et al., 2006

[†]Location shown in Figure 8